Materials Advances

Accepted Manuscript

This article can be cited before page numbers have been issued, to do this please use: M. U. Salman, M. M. Mudassar, M. Arshad, M. Luqman, M. Mehak, M. Atif, M. Asim and S. Atiq, *Mater. Adv.*, 2026, DOI: 10.1039/D6MA00329J.

ROYAL SOCIETY OF CHEMISTRY

rsc.li/materials-advances

View Article Online
DOI: 10.1039/D6MA00329J

Optimization of ultrathin Mg-doped ZnO layer for efficient charge carrier extraction in $BiFeO_3$-based solar cells

Muhammad Umar Salman[1], Muhammad Mubeen Mudassar[1], Mehwish Arshad[1], Muhammad Luqman[1], Muhammad Mehak[1], Muhammad Atif[2], Muhammad Asim[3], Shahid Atiq[1,*]

[1]*Centre of Excellence in Solid State Physics, University of the Punjab, Lahore-54590, Pakistan*
[2]*Physics and Astronomy Department, College of Science, P.O. Box 2455, King Saud University, Riyadh 11451, Saudi Arabia*
[3]*Department of Physics and Astronomy, Sejong University, Seoul, South Korea*

Abstract

As the world moves towards more sustainable energy, research into multifunctional oxide-based solar cell designs presents promising alternatives to established technology. In this study, a one-dimensional single-junction device structure, Mg-doped ZnO (MZO)/$BiFeO_3$ (BFO)/Cu_2FeSnS_4 (CFTS) was numerically simulated using COMSOL Multiphysics, aiming to analyze its optoelectronic behavior under varied physical conditions. The core absorber (BFO) was chosen for its unique integration of ferroelectricity, magnetism, and suitable bandgap properties, which enhance charge separation and light absorption processes. The device achieved a maximum short-circuit current density of 8.96 mA cm^{-2} at a donor density of 1×10^{16} cm^{-3}, while the highest open-circuit voltage of 0.93 V was observed at 250 K. Notably, a fill factor of 78.99% was recorded at 390 K, and the optimum efficiency of 5.45% emerged at 285 K under a donor density of 1×10^{18} cm^{-3}. These results suggest strong potential for oxide-based multiferroic absorbers in future photovoltaic platforms, particularly for stable, temperature-resilient, and environmentally sustainable energy applications.

Keywords: COMSOL Multiphysics; Lead free perovskites; Solar cell simulation; $BiFeO_3$; Renewable energy

Corresponding authors: *Muhammad Umar Salman (muhammadumarsalmanm@gmail.com); **Shahid Atiq (satiq.cssp@pu.edu.pk)

View Article Online
DOI: 10.1039/D6MA00329J

1. Introduction

The escalating global demand for energy has placed immense pressure on conventional fossil fuel resources, accelerating environmental degradation and greenhouse gas emissions. The widespread reliance on fossil fuels has not only led to significant carbon dioxide emissions but also contributed to climate instability and resource depletion. Reports indicate that in 2021, worldwide electricity usage experienced a sharp rise of approximately 45%, corresponding to nearly 1000 terawatt-hours, underscoring the pressing demand for clean and reliable energy alternatives [1, 2]. Addressing this challenge, international energy frameworks emphasize that transitioning to renewable sources is vital to halving global carbon emissions by mid-century, thereby helping limit average temperature rise to within safe thresholds near 2 °C [3]. Among available options, solar energy stands out for its abundance and low environmental impact, with photovoltaic (PV) technologies making notable progress [4, 5]. The incorporation of toxic lead in perovskite-based solar cells (PSCs) remains a critical drawback, thereby motivating research toward safer, lead-free alternatives that maintain performance while ensuring environmental compatibility. To realize the full potential of lead-free perovskite-inspired absorbers, it is imperative to design an appropriate solar cell architecture that supports efficient charge generation and transport.

To develop efficient and environmentally friendly PV devices, the choice of absorber material is critical. $BiFeO_3$ (BFO), a lead-free multiferroic oxide, has garnered considerable interest due to its unique combination of ferroelectric and semiconducting properties [6-8]. Its suitable bandgap, typically around 2.1-2.7 eV, enables visible light absorption, while its intrinsic polarization facilitates efficient charge separation [9-12]. Moreover, BFO offers excellent thermal and chemical stability, making it a robust candidate for long-term solar cell operation [13, 14]. These attributes collectively position BFO as a promising absorber layer in next-generation, non-toxic solar cell architectures. To complement the absorber layer, an effective electron transport layer (ETL) is essential for facilitating charge extraction and minimizing recombination losses. 1-3 wt% Magnesium-doped zinc oxide (MZO), a tunable wide bandgap (3.33 eV) semiconductor, serves this role effectively due to its high transparency, and excellent electron mobility [15]. By adjusting the Mg content, the energy band alignment with the absorber layer can be optimized, enhancing charge transfer efficiency. Additionally, MZO exhibits strong chemical stability and

View Article Online
DOI: 10.1039/D6MA00329J

low-temperature processability, making it suitable for scalable fabrication. Cu_2FeSnS_4 (CFTS) has gained attention as a potential hole transport layer (HTL) due to its non-toxic composition, earth-abundant elements, good bandgap (1.3 eV), and favorable optoelectronic properties [16]. Its suitable valence band alignment with common absorber materials enables efficient hole extraction and transport while minimizing energy loss.

Several solar cell configurations have been explored in recent years to enhance performance through material optimization. Kaur *et al*. (2017) reported a Cr/ITO/Cu_2O/ MZO/AZO-based device achieving an efficiency of 1.62%, while Deepika *et al*. (2023) demonstrated an FTO/ZnO/CdS/CFTS architecture with 1.32% efficiency [17, 18]. Raj *et al*. (2024) introduced a BFO-based configuration, FTO/ZnO/BFO/Spiro-OMeTAD/Au, which reached a relatively improved efficiency of 1.92% [19]. However, these designs either suffer from limited output or rely on toxic or less stable materials. In contrast, the present study proposes an MZO/BFO/CFTS structure, integrating a stable, non-toxic absorber and optimized interface materials, resulting in a significantly enhanced efficiency of 5.45%. This notable improvement highlights the potential of the proposed architecture to overcome existing limitations and bridge the performance gap in environmentally sustainable solar cell research.

The novelty of this work lies in the strategic integration of MZO/BFO/CFTS layers modeled through one-dimensional simulations using COMSOL Multiphysics, enabling detailed analysis of electrical and optoelectronic behavior across varying device parameters. This simulation-driven approach facilitates precise control over layer properties, revealing key performance insights often difficult to obtain experimentally. By achieving enhanced efficiency with entirely non-toxic, earth-abundant materials, this study contributes to the ongoing shift toward environmentally responsible solar technologies. The findings serve as a foundation for future experimental fabrication and suggest broad potential for tailored PV designs aimed at efficient, scalable, and sustainable energy solutions.

2. Numerical Modelling

To simulate the coupled electro-optical behavior and carrier transport within the solar cell device, numerical modeling was carried out using COMSOL Multiphysics, a finite element simulation platform that allows self-consistent solutions of the Poisson equation, carrier continuity

View Article Online
DOI: 10.1039/D6MA00329J

equations, and current density formulations. The fundamental governing equations of the device physics are described below. The electrostatic potential distribution ($\partial\varphi$) is determined by the Poisson equation (Eq. 1), which relates the electric field to the space charge density within the semiconductor [20]:

$$\frac{\partial}{\partial x}\left(\varepsilon_0\varepsilon_r\frac{\partial\varphi}{\partial x}\right) = -e(N_D^+ - N_A^- + p - n + \frac{\rho_{def}}{e}) \quad (1)$$

Here, in Eq. 1, ε_0 is the vacuum permittivity, ε_r is the relative permittivity of the material, $\partial\varphi$ is the electrostatic potential, and e is the elementary charge. N_D^+ and N_A^- represent the ionized donor and acceptor concentrations, respectively. Furthermore, n and p represent the free electron and hole (e-h) concentrations, while ρ_{def} accounts for any fixed defect charge density in the device. The time evolution of e-h densities, accounting for generation, recombination, and carrier transport, is governed by the continuity equations (Eqs. 2 & 3), while associated drift-diffusion current densities for e-h (Eqs. 4 & 5) under the quasi-Fermi level gradient formulation are given by:

$$G_n - U_n - \frac{\partial J_n}{\partial x} = \frac{\partial n}{\partial t} \quad (2)$$

$$G_p - U_p - \frac{\partial J_p}{\partial x} = \frac{\partial p}{\partial t} \quad (3)$$

$$J_n = \frac{\mu_n n \partial E_{Fn}}{e \quad \partial x} \quad (4)$$

$$J_p = \frac{\mu_p p \partial E_{Fp}}{e \quad \partial x} \quad (5)$$

In these Eqs. 2, 3, 4, & 5, G_n and G_p are the e-h generation rates, and U_n, U_p are their corresponding recombination rates. μ_n and μ_p denote the mobilities of e-h, E_{Fn} and E_{Fp} are the quasi-Fermi levels, and $\partial/\partial x$ represents the spatial derivative along the device thickness [20-23]. These equations are simultaneously solved to analyze transient or steady-state carrier behavior and net current flow under illumination. The depth-resolved photogeneration profile G(x) (Eq. 6) across the absorber layer is obtained by integrating the wavelength-dependent generation rate over the relevant spectral range of the incident light [24, 25]:

View Article Online
DOI: 10.1039/D6MA00329J

$$G(x) = \int_{\lambda_{min}}^{\lambda_{max}} G(\lambda,x)d\lambda = \int_{\lambda_{min}}^{\lambda_{max}} \alpha(\lambda), N_{phot}(\lambda,x)d\lambda \quad (6)$$

Here, in Eq. 6, $\alpha(\lambda)$ is the absorption coefficient at wavelength (λ), and $N_{phot}(\lambda,x)$ is the photon flux at depth x. The integration limits λ_{min} and λ_{max} correspond to the spectral response of the active material, typically derived from the solar AM1.5G spectrum. Carrier recombination via trap-assisted processes is modeled using the Shockley-Read-Hall recombination (R_{SRH}) rate (Eq. 7), which captures the influence of deep-level traps in the bandgap [26]:

$$R_{SRH} = \frac{np - n_i^2}{r(p+n+2n_i\cosh\left(\frac{E_i - E_t}{kT}\right))} \quad (7)$$

In Eq. 7, n_i is the intrinsic carrier concentration, τ is the effective carrier lifetime, E_i is the intrinsic Fermi level, and E_t is the trap energy level. The term kT denotes the thermal energy, where k is Boltzmann's constant and T is the absolute temperature. This equation (Eq. 7) is critical for understanding non-radiative recombination losses in the absorber and interface layers. This numerical framework, executed through COMSOL's Multiphysics environment, enables detailed resolution of spatial variations in potential, carrier density, generation-recombination dynamics, and current distribution, ultimately guiding the optimization of solar cell performance parameters. The current density in the device is described by the modified Shockley diode equation (Eq. 8):

$$J = J_{ph} - J_o\left[\exp\left(\frac{qV}{nkT}\right) - 1\right] \quad (8)$$

Here, in Eq. 8, J denoted the total current density, while J_{ph} represents the photogenerated current density. The ideality factor is given by n, which accounts for deviation from ideal diode behavior due to recombination mechanisms. J_o is the reverse saturation current density, and q, k, and T correspond to the elementary charge, Boltzmann constant, and absolute temperature, respectively. The open-circuit voltage (V_{oc}) was extracted numerically from the COMSOL Multiphysics simulated J-V characteristics under illumination by imposing the open-circuit condition J=0. Under this condition, Eq. 8 can be rearranged to express V_{oc} as:

$$V_{oc} = \frac{nTk}{q}\left[\ln\left(\frac{J_{sc}}{J_o} + 1\right)\right] \quad (9)$$

View Article Online
DOI: 10.1039/D6MA00329J

Here, in Eq. 9, J_{sc} represents the short-circuit current density (J_{sc}) and V_{oc} denotes the open circuit voltage [27]. The numerically obtained V_{oc} values from COMSOL remain below the theoretical limit imposed by the absorber bandgap of BFO, which is primarily attributed to charge carrier recombination losses and intrinsic voltage deficits commonly observed in oxide-based PV systems.

3. Device Simulation and Methodology

3.1 Spectral Irradiance and Photonic Energy Harvesting

Fig. 1(a) illustrates the spectral distribution of solar irradiance as a function of wavelength under standard AM 1.5G conditions, representing the solar energy received on the Earth's surface after passing through 1.5 times the atmospheric path length. The curve spans the ultraviolet, visible, and near-infrared regions, with maximum intensity centered around 450 nm, indicating that the visible region carries the majority of solar power [28]. This standardized spectrum is widely used in various scientific and technological fields including atmospheric studies, optical engineering, biological modeling, and renewable energy simulations, as it provides a reference for how sunlight is spectrally distributed under typical daylight conditions. The spectral shape resembles the blackbody radiation of the sun at an effective temperature of approximately 5778 K, and its accurate representation is essential for analyzing light-matter interactions, energy absorption profiles, and system performance that depend on solar exposure across different wavelength ranges. Fig. 1(b) illustrates the spatial distribution of the photogeneration rate along the arc length of the device. The graph shows that photogeneration is highest near the illuminated surface and gradually decreases with increasing depth due to the attenuation of light as it passes through the material. This variation highlights how the penetration and absorption of incident light influence carrier generation across the device geometry, which is critical for optimizing device performance. Fig. 1(c) presents the R_{SRH} rate along the arc length of the active layer, the rate rises sharply near the beginning, peaking around 300 nm, and then steadily decreases towards the end of the arc. This indicates that trap-assisted recombination is most prominent near the front region of the device, possibly due to higher defect density or stronger carrier interaction in that zone, which can adversely affect carrier lifetime and device efficiency. Fig. 1(d) depicts that the absorption coefficient along the arc length is notably high when the incident wavelength ranges

View Article Online
DOI: 10.1039/D6MA00329J

between 0.3 μm and 0.5 μm, reflecting strong absorption of high-energy photons in the visible region. Beyond this range, the coefficient drops sharply, indicating diminished absorption efficiency at longer wavelengths. This trend underscores the material's suitability for capturing photons in the shorter wavelength region of the solar spectrum [29].

Fig. 2(a) presents a detailed schematic of the solar cell architecture, highlighting the layered arrangement crucial for optimized photoelectric conversion. The configuration begins with a front transparent electrode, enabling light entry, followed by an ETL that facilitates electron extraction. The central absorbing layer captures incident photons to generate electron-hole pairs, while the adjacent HTL selectively moves holes towards the back contact. This systematic stacking not only minimizes recombination but also supports efficient charge separation and collection, thereby enhancing the PV response of the device [30]. Fig. 2(b) displays the simulated electric field distribution across the device layers, indicating how effectively the built-in field assists in charge separation. A strong, uniform field is observed near the junction regions, particularly within the absorber and adjoining transport layers, which plays a crucial role in driving photo-generated carriers toward their respective electrodes. This spatial distribution reflects optimal device design, ensuring reduced carrier recombination and promoting efficient current extraction under illumination. Fig. 2(c) presents the energy band alignment of the device layers, clearly indicating the stepwise variation in conduction band (CB) and valence band (VB) edges across the heterojunction. The CB minimum exhibits a favorable downhill path from the ETL toward the absorber and then to the HTL, ensuring efficient electron extraction. Similarly, the upward slope in the VB promotes hole transport in the opposite direction. This alignment minimizes recombination and facilitates effective charge separation, which is critical for optimizing overall photovoltaic performance [31-33]. The key material parameters used for simulation in COMSOL, including bandgap, dielectric constant, and mobility values for each layer, are summarized in Table 1.

Table 1 presents the principal material parameters assigned to each functional layer of the device, which together define its electronic characteristics and charge transport behavior. The physical thickness of each layer determines the optical path length and has a direct impact on light absorption, carrier transport routes, and the likelihood of recombination within the device. The bandgap is a fundamental property governing the optical response of each layer and is crucial for

View Article Online
DOI: 10.1039/D6MA00329J

establishing the energy band alignment, a key benchmark for assessing overall device operation. Electron affinity specifies the energy separation between the conduction band minimum and the vacuum level and is vital for enabling efficient extraction of photogenerated electrons across material interfaces. Relative permittivity characterizes the polarization response of each layer and influences the screening of Coulomb interactions, thereby affecting the separation and stability of photogenerated charge carriers. The density of states describes the availability of electronic states near the band edges for electrons and holes, playing an important role in determining carrier concentrations and recombination processes. Electron and hole mobilities indicate how readily charge carriers move through their respective layers under an applied electric field and therefore strongly influence current flow and series resistance. Carrier lifetime denotes the average time photogenerated carriers persist before recombination and is a critical parameter for effective charge collection. Taken together, these parameters offer a complete physical description of the device architecture and ensure that the simulated results are based on realistic material properties and transport mechanisms.

4. Results and Discussion

4.1 Impact of BFO's Absorber Layer Thickness on PV Parameters

Fig. 3(a) illustrates the schematic comparison of photogeneration rate as a function of BFO absorber layer thickness, where a thinner layer results in reduced carrier generation due to limited light absorption and shorter interaction depth within the material. As the thickness increases, more incident photons are absorbed over the extended optical path, leading to a higher generation rate and improved charge carrier density, although beyond a certain point, further thickness may lead to slight recombination losses or transport limitations. Fig. 3(b) displays the J-V characteristics, where the J_{sc} increases consistently with the rise in BFO absorber layer thickness, indicating improved light absorption and enhanced carrier generation due to the presence of more active material. At the microscopic level, the enhancement in J_{sc} with BFO absorber layer thickness indicate an improved optical absorption due to extended photon path length within the active layer. The increased thickness enhances light-matter interaction, allowing a greater number of incident photons to be absorbed and subsequently convert into photogenerated charge carriers, thereby contributing to an overall increase in J_{sc}. Despite the increase in J_{sc}, the current density at V_{oc} remains nearly unchanged, suggesting that the electric field and recombination behavior are not

View Article Online
DOI: 10.1039/D6MA00329J

significantly affected. At the microscopic scale, the bulk recombination centers and Shockley-Read Hall recombination remain approximately invariant with respect to thickness variation. Consequently, the overall shape of the characteristics curve reflects a stable diode behavior, indicating that the fundamental recombination mechanisms are not significantly altered by change in the absorber layer thickness. Fig. 3(c) illustrates the variation in power output with voltage for different BFO absorber layer thicknesses, where thicker layers clearly shift the P-V curve upward, reflecting a stronger energy conversion response. The enhanced area under the curve with increasing thickness indicates a higher usable power range, showing that the device becomes more effective at converting incident light into electrical power without altering its operational stability or introducing nonlinearity in the output response.

Fig. 3(d) presents the numeric values of J_{sc}, V_{oc}, and maximum power output (P_{max}) with increasing BFO absorber layer thickness, where J_{sc} rises from 4.77 mA cm^{-2} at 100 nm to 8.92 mA cm^{-2} at 1700 nm, reflecting a significant improvement in carrier generation due to enhanced light absorption [37, 38]. V_{oc} shows a slight decline from 0.89 to 0.84 V across the same range, which is minor and does not greatly affect performance. Correspondingly, P_{max} increases from 28.03 to 49.09 W m^{-2}, confirming that the overall power output benefits notably from thickness optimization despite a modest voltage drop. Fig. 3(e) shows that both fill factor (FF) and efficiency exhibit a gradual increase with BFO absorber layer thickness, where FF remains relatively stable around 65%, indicating that internal losses and charge extraction quality are consistent across all thicknesses. The steady rise in efficiency from 2.80 to 4.90% reflects the cumulative impact of improved generation rate and current output, confirming that optimizing absorber thickness is a key factor in enhancing overall device performance without compromising structural or electrical integrity [39, 40]. Table 2 clearly reflects a positive performance trend with increasing absorber thickness, highlighting that device output improves steadily without major compromise in operational stability or internal balance.

4.2 Effect of ETL Thickness on PV Parameters

Fig. 4(a) illustrates the effect of ETL thickness on electron extraction, where at lower thicknesses, carriers are efficiently extracted due to shorter transport paths and reduced resistance, resulting in minimal recombination losses. As the ETL becomes thicker, electron extraction

View Article Online
DOI: 10.1039/D6MA00329J

weakens because the increased distance and resistance hinder carrier mobility, leading to delays and possible recombination before reaching the contact, ultimately reducing overall device performance. Fig. 4(b) shows the J-V curves, where increasing the ETL thickness leads to a clear reduction in current density, as thicker layers introduce higher resistance and longer transport paths, making it harder for electrons to reach the electrode efficiently. Although the V_{oc} remains nearly constant across all thicknesses, the noticeable drop in current at each voltage point reflects weaker carrier extraction and increased recombination in thicker ETLs. Fig. 4(c) displays the P-V curves, where increasing ETL thickness results in a progressive decrease in output power, primarily due to reduced current flow through the device. The shape of the curves remains consistent, but the peak power shifts downward with thickness, confirming that excessive ETL thickness limits charge transport efficiency without significantly affecting the voltage operating range.

Fig. 4(d) presents the variation in J_{sc}, V_{oc}, and P_{max} with increasing ETL thickness, where J_{sc} declines from 8.92 to 5.83 mA cm^{-2} and P_{max} drops from 49.05 to 32.24 W m^{-2}, as the ETL thickness increases from 10 to 130 nm, mainly due to longer electron transport paths and higher series resistance, which hinder efficient carrier collection and increase transport losses. V_{oc} remains nearly constant (0.83-0.85 V) across all thicknesses, as it is primarily governed by the built-in potential and recombination rate, which are only weakly affected by ETL thickness variations within this range [41]. Fig. 4(e) shows that both FF and efficiency gradually decrease with increasing ETL thickness, where FF drops slightly from 65.94 to 64.53% and efficiency declines from 4.90 to 3.22%, reflecting the cumulative impact of reduced charge extraction and increased resistive losses [42, 43]. The decline in efficiency is mainly driven by the drop in J_{sc} and P_{max}, while the relatively stable FF suggests that the internal device architecture remains intact but becomes less effective at transporting charges at higher ETL thicknesses. Table 3 highlights the downward trend in device performance with increasing ETL thickness, indicating that thicker layers negatively impact charge transport and overall efficiency without significantly altering voltage stability.

View Article Online
DOI: 10.1039/D6MA00329J

4.2 Effect of HTL Thickness on PV Parameters

Fig. 5(a) illustrates a schematic comparison of hole extraction behavior at different HTL thicknesses, where thinner layers result in less efficient hole transport due to insufficient material coverage and weaker field-driven separation near the interface. As the HTL thickness increases, hole extraction improves noticeably because of better interfacial contact and a stronger driving field for carrier collection, which helps minimize recombination and ensures more efficient charge transfer toward the back electrode. Fig. 5(b) shows the J-V characteristics for varying HTL thicknesses, where current density remains nearly stable across all thicknesses, but the curve for higher thicknesses shifts slightly toward higher voltage, indicating improved built-in potential and reduced recombination. This slight voltage gain reflects enhanced hole transport and collection efficiency at greater HTL thickness without compromising the current output. Fig. 5(c) presents the P-V curves, where the peak power output gradually shifts upward and slightly toward higher voltage as HTL thickness increases, reflecting better energy conversion capability. The enhancement in power output suggests that thicker HTLs support more efficient charge extraction and reduce energy losses during transport, leading to a stronger and more stable output response.

Fig. 5(d) presents that with increasing HTL thickness, J_{sc} remains steady from 8.92 mA cm^{-2} at 10 nm to 8.95 mA cm^{-2} at 130 nm, showing minimal influence of HTL thickness on current generation [44]. In contrast, V_{oc} increases from 0.83 to 0.89 V, and P_{max} rises from 49.05 to 53.92 W m^{-2} across the same range, indicating improved charge separation and reduced recombination losses due to enhanced hole transport in thicker HTLs. Fig. 5(e) shows that as HTL thickness increases from 10 to 130 nm, the FF improves slightly from 65.82 to 67.42%, while efficiency increases from 4.90 to 5.39%. This upward trend reflects enhanced hole extraction and reduced series resistance, which together contribute to more efficient charge collection and overall better device performance. Table 4 reflects the positive impact of increasing HTL thickness on overall device performance, showing steady enhancement in output parameters without compromising generation stability or introducing significant internal losses.

View Article Online
DOI: 10.1039/D6MA00329J

4.4 Effect of Donor Density Variation on PV Parameters

Fig. 6(a) illustrates the J-V behavior of the solar cell under different donor density (N_D) levels in the ETL. With increasing N_D, a pronounced improvement in the shape of the J-V curves is observed, indicating enhanced charge carrier collection, improved electrical conductivity, and reduced series resistance. This behavior is attributed to more efficient electron transport toward the front electrode, facilitated by the increased availability of free charge carriers. Higher doping concentration also modifies the band bending at the ETL/BFO interface, resulting in improved band alignment and an enhanced built-in electric field. This strengthened electric field promotes more effective separation of electron-hole pairs, thereby significantly suppressing the probability of bulk recombination. Furthermore, the reduction in recombination at higher N_D suggests improved electrostatic screening, which diminishes the influence of defect state within the ETL. As a consequence, carrier lifetime and collection efficiency at the front electrode are enhanced ultimately leading to the observed improvement in the overall J-V curve characteristics. Fig. 6(b) presents P-V characteristics of the device at varying N_D in the ETL, when N_D increases, the output power curves exhibit a marked enhancement in peak power, suggesting more efficient photo-generated charge extraction. This improvement reflects the optimized balance between charge transport and reduced resistive losses, leading to a more favorable operating point. Fig. 6(c) shows that J_{sc} remains stable around 8.96 mA cm^{-2} as N_D increases, indicating that light absorption and photogeneration are unaffected. V_{oc} increases slightly from 0.87 to 0.89 V due to reduced recombination from enhanced built-in electric field. P_{max} increases notably from 33.60 to 54.53 W m^{-2}, reflecting improved charge extraction and reduced series resistance [45]. Fig. 6(d) reveals that FF improves from 42.79 to 68.57% and efficiency from 3.36 to 5.45% with increasing N_D. This is because higher N_D enhances conductivity, minimizes carrier recombination, and strengthens the junction field, resulting in more efficient charge collection and improved device performance. The results in Table 5 confirm that performance progressively improves with increasing N_D, indicating more efficient charge transport and reduced recombination, while one key output remains nearly unchanged across all values.

View Article Online
DOI: 10.1039/D6MA00329J

4.5 Effect of Temperature Variation on PV Parameters

Fig. 7(a) presents a schematic representation of how temperature affects the device operation. At lower temperatures, the lattice vibrations remain within an optimal range, minimizing phonon scattering and allowing efficient charge transport, which enhances overall performance. In contrast, as the temperature rises, excessive thermal agitation increases recombination rates and disrupts carrier mobility, resulting in decreased efficiency. The J-V characteristics in Fig. 7(b) illustrate temperature-dependent behavior. At lower temperatures, the J-V curve maintains higher voltage stability, with the current density starting to decline near 0.7 V. However, at elevated temperatures, this decline begins earlier, around 0.6 V, indicating increased carrier recombination and reduced voltage output. This behavior can be attributed to thermally activated recombination mechanism. As the temperature increase, enhanced lattice vibrations intensify electron-phonon interactions, leading to increase scattering. This scattering reduces charge carrier mobility and elevates transport resistance within the device. Moreover, elevated temperature thermally activates deep-level trap states and defect-assisted SRH recombination centers, thereby increasing the probability of non-radiative recombination before carrier collection. Consequently, carrier lifetime decreases and recombination losses become more pronounced. In contrast, at lower temperatures, suppressed phonon interactions reduce carrier scattering and limit the activation of defect states. This results in enhanced carrier mobility, prolonged carrier lifetime, and improved voltage stability. The reduction in recombination losses delays the onset of current saturation in the J-V curve, thereby preserving device performance under reduced thermal conditions. The P-V curves in Fig. 7(c) show that at lower temperatures, the device maintains higher power over a broader voltage range, indicating efficient charge extraction and reduced recombination. As the temperature rises, the maximum power point shifts to lower voltages, and the overall power output declines.

Fig. 7(d) depicts that with rising temperature from 250 to 390 K, the V_{oc} drops from 0.93 V to 0.71 V and the P_{max} decreases from 54.20 to 50.89 W m^{-2}, while the J_{sc} remains constant at 8.96 mA cm^{-2}. This suggests that temperature negatively affects device performance by lowering the voltage and power output despite stable current generation [46-48]. Fig. 7(e) shows that as temperature increases from 250 to 285 K, FF rises from 64.89 to 68.52%, and efficiency peaks at 5.45%, indicating improved charge extraction and reduced resistive losses. However, beyond

View Article Online
DOI: 10.1039/D6MA00329J

285 K, FF continues to increase slightly up to 78.99% at 390 K, while efficiency declines to 5.08%, suggesting that higher FF alone cannot compensate for losses caused by reduced V_{oc} and enhanced recombination at elevated temperatures [33, 43, 49]. Table 6 tabulates the variation in device performance, showing initial enhancement followed by a gradual decline under increasing external stress, consistent with graphical trends.

Table 7 presents a comparative evaluation of photovoltaic performance metrics for various BFO-based solar cell architectures reported in the literature. The FTO/ZnO/BFO/spiro-OMeTAD/Au configuration yielded a J_{sc} of 8.35 mA cm^{-2} and a V_{oc} of 0.79 V; however, its poor fill factor (29.10%) significantly limited efficiency to only 1.92% [19]. The TiO_2/BFO/NiO device exhibited even lower J_{sc} (0.51 mA cm^{-2}) and efficiency (0.19%) despite a relatively better FF of 55%, reflecting suboptimal carrier extraction and limited photogeneration [50]. On the other hand, the Graphite/BFO/ZnO/ITO structure showed the highest J_{sc} (12.47 mA cm^{-2}) among all references but was hindered by a low V_{oc} (0.64 V) and moderate FF (50.4%), resulting in a maximum efficiency of 3.98% [51].

Experimentally, the FTO/BFO/GO device architecture exhibited a very low efficiency of 0.02%, accompanied by a J_{sc} of 0.134 mA cm^{-2}, indicating limited charge generation and inefficient carrier extraction [52]. Upon modification of the contact configuration by replacing the front and back contacts with ITO and Al, respectively, the Al/BFO/ITO structure demonstrated a significant improvement efficiency of 0.89% [53]. Furthermore, a BFO-based multilayer architecture comprising ITO/ZnO-u/BFO/Al yielded the highest device performance, delivering a maximum J_{sc} of 4.7 mA cm^{-2} and corresponding efficiency of 2.21%. This substantial enhancement suggests improved interfacial charge transport, reduced recombination losses, and more efficient carrier collection due to optimized electrode ad transport layer engineering [54].

In comparison, the MZO/BFO/CFTS device developed in this work demonstrates superior and well-balanced PV parameters. It achieves a J_{sc} of 8.96 mA cm^{-2}, a significantly high V_{oc} of 0.93 V, and a remarkably improved FF of 78.99%, leading to the highest overall efficiency of 5.45%. This indicates enhanced charge carrier transport, effective suppression of recombination, and optimized energy band alignment across interfaces. The novelty of this work stems from the strategic integration of MZO/CFTS/BFO materials, unlike conventional architectures, this unique

View Article Online
DOI: 10.1039/D6MA00329J

combination ensures broader spectral absorption, better carrier mobility, and environmentally benign composition. Moreover, the improved built-in electric field and energy band offsets facilitate efficient photogenerated carrier separation and extraction, which collectively enhance device performance. Thus, this work not only surpasses earlier BFO-based solar cell designs in terms of photovoltaic output but also introduces a cost-effective, non-toxic, and scalable architecture, offering a promising route for future-generation energy harvesting technologies.

Table 8 presents a comprehensive analysis of the BFO-based device architecture investigated in this study, incorporating optimized structural and operational parameters. The thicknesses of the BFO absorber layer, ETL, and HTL were systematically optimized to 1700 nm, 10 nm, 130 nm, respectively, to achieve enhanced photovoltaic performance. Moreover, the device exhibited performance under a donor density of 1×10^{20} cm^{-3} and an operating temperature of 285 K. These conditions collectively contributed to improved charge transport, reduced recombination losses, and enhanced overall device efficiency.

4.6 Resistance analysis

Fig. 8(a) schematically illustrates the origin of parasitic resistive components in the device architecture. The series resistance (R_s) primarily arises from interfacial defects and imperfect contact formation b/w adjacent layers, particularly at the MZO/BFO and BFO/CFTS interfaces, whereas the shunt resistance (R_{sh}) is associated with internal fractures, pinholes, and structural imperfections within the individual layers that facilitate leakage current pathways. Fig. 8(b) presents the variation of R_s, R_{sh}, and characteristics resistance (R_{ch}) as a function of BFO absorber layer thickness, varied from 100 to 1700 nm. The minimum R_s (0 Ω-cm^2) is observed at a lower BFO absorber layer thickness (100 nm), indicating reduced bulk recombination and efficient charge carrier transport due to shorter diffusion pathways. As the BFO absorber layer thickness increases, Rs gradually rises, reaching a maximum value of approximately 2.8 Ω-cm^2 at 1700 nm. This increase can be attributed to enhanced bulk recombination, increased defect density, and prolonged carrier transport distance within the thicker absorber. Conversely, the maximum R_{sh} (~34,000 Ω-cm^2) is obtained at 1700 nm, suggesting suppressed leakage current and relatively reduced recombination via shunt pathways. The overall device resistance, represented by R_{ch}, reflects the combined resistive contribution of all layers. The minimum R_{ch} (~270 Ω-cm^2) at

View Article Online
DOI: 10.1039/D6MA00329J

maximum absorber thickness indicates improved overall structural integrity and balanced charge transport across the device stack [6].

Fig. 8(c) illustrates the dependence of R_s, R_{sh}, and R_{ch} on the ETL thickness and the minimum R_s (~6.5 Ω-cm^2) is achieved at an ETL thickness of 10 nm, which can be attributed to enhanced charge extraction efficiency and reduced interfacial recombination. Similarly, the optimal R_{sh} (~11,000 Ω-cm^2) at 10 nm suggests minimized internal defect states and suppressed leakage current. Furthermore, the lowest R_{ch} (~265 Ω-cm^2) observed at this thickness indicates reduced structural imperfections and efficient carrier transport across the heterojunction. Fig. 8(d) depicts the influence of HTL thickness on the resistive parameters. At a higher HLT thickness of 130 nm, R_s reaches its maximum value (~3.60 Ω-cm^2), reflecting increased recombination losses and higher defect density within the thicker transport layer. Interestingly, R_{sh} also attains a relatively high value (~9800 Ω-cm^2) at 130 nm, indicating reduced leakage current and improved R_{sh} despite the increased R_s. Moreover, the comparatively low R_{ch} (~246 Ω-cm^2) at higher HTL thickness suggests that the overall device maintains efficient charge transport with minimized recombination through alternative pathways [55].

Fig. 8(e) demonstrates the variation of R_s, R_{sh}, and R_{ch} as a function of N_D, varied from 1×10^{15} to 1×10^{20} cm^{-3}. The minimum R_s (~3.5 Ω-cm^2) is obtained at higher donor concentration (~1×10^{20} cm^{-3}), which can be attributed to improved electrical conductivity and enhanced crystalline quality, leading to reduced recombination losses. Correspondingly, R_{sh} reaches a higher value (~9500 Ω-cm^2) at elevated N_D, indicating suppressed leakage current and lower defect-assisted recombination. Additionally, the minimum R_{ch} (~245 Ω-cm^2) at higher N_D further confirms improved charge transport characteristics and reduced overall resistive losses. Fig. 8(f) presents the temperature dependence of R_s, R_{ch}, and R_{sh} over the range of 250-390 K. The maximum R_s (~4 Ω-cm^2) is observed at elevated temperatures, indicating increased interfacial and phonon-assisted recombination process. In contrast, the maximum R_{sh} (~11,000 Ω-cm^2) occurs at 250 K, suggesting lower defect activation and reduced recombination at lower temperature. The minimum R_{ch} (~246 Ω-cm^2) is also recorded at lower temperature, while R_{ch} gradually increases with rising temperature, reaching a maximum value (~257 Ω-cm^2) around 390 K. This trend reflects thermally activated carrier scattering and enhanced recombination dynamics at higher operating temperatures.

View Article Online
DOI: 10.1039/D6MA00329J

5. Conclusion

A comprehensive numerical simulation was conducted using COMSOL Multiphysics for the MZO/BFO/CFTS solar cell configuration, with the objective of analyzing the effects of structural and operational parameters on overall device performance. The variation in BFO absorber layer thickness from 100 to 1700 nm resulted in a significant increase in short-circuit current density (J_{sc}) from 4.77 to 8.92 mA cm^{-2} and an improvement in efficiency from 2.80 to 4.90%, although a slight reduction in open-circuit voltage (V_{oc}) and fill factor (FF) was observed due to increased carrier recombination. Increasing the electron transport layer thickness from 10 to 130 nm led to a decline in J_{sc} and efficiency from 8.92 to 5.83 mA cm^{-2} and 4.90 to 3.22% respectively, primarily due to higher resistance and reduced carrier extraction. In contrast, varying the hole transport layer thickness within the same range resulted in a modest but consistent enhancement in all performance parameters, raising efficiency from 4.90 to 5.39% as a result of improved hole mobility and interface quality. When the donor density was varied from 1×10^{15} to 1×10^{20} cm^{-3}, both J_{sc} and V_{oc} remained nearly constant, but a substantial increase in FF from 42.79 to 68.57% led to an efficiency rise from 3.36 to 5.45%, indicating improved internal charge transport. Under thermal analysis, as the temperature increased from 250 to 390 K, J_{sc} remained stable, but V_{oc} decreased from 0.93 to 0.71 V, resulting in a slight drop in efficiency from 5.42 to 5.08% due to elevated recombination rates, although FF improved with temperature. Furthermore, the resistance analysis based on Python software validates the role of parasitic resistances in photovoltaic efficiency variation. These findings confirm that the MZO/BFO/CFTS structure holds strong potential as a stable and lead-free photovoltaic device, and that targeted optimization of material thickness and doping conditions can substantially enhance its power conversion efficiency for future solar energy applications.

Conflict of Interests:

The authors declare that there are no financial or any other types of conflicts of interests to declare for this submission.

Data Availability Statement:

The data will be available on request.

View Article Online
DOI: 10.1039/D6MA00329J

Acknowledgement:

The authors extend their sincere appreciation to the Ongoing Research Funding program, (ORF-2026-397), King Saud University, Riyadh, Saudi Arabia for the financial support.

References

1. A. Raj, M. Kumar, A. Kumar, K. Singh, S. Sharma, R. C. Singh, M. S. Pawar, M. Z. A. Yahya and A. Anshul, *Ceramics International*, 2023, 49, 1317–1327.
2. S. Sarker, M. T. Islam, A. Rauf, H. Al Jame, M. R. Jani, S. Ahsan, M. S. Islam, S. S. Nishat, K. M. Shorowordi and S. Ahmed, *Solar Energy*, 2021, 225, 471–485.
3. J. Gao and L. Zhang, *Journal of the Asia Pacific Economy*, 2021, 26, 96–115.
4. A. S. Al-Ezzi and M. N. M. Ansari, *Applied System Innovation*, 2022, 5, 67.
5. N. S. Kumar and K. C. B. Naidu, *Journal of Materiomics*, 2021, 7, 940–956.
6. M. M. Mudassar, M. Arshad, M. U. Salman, A. Mahmood, W. Al-Masry, M. Asim and S. Atiq, *RSC Advances*, 2025, 15, 33830–33843.
7. J. S. Bangruwa, B. K. Vashisth, N. Singh and V. Verma, *Ceramics International*, 2018, 44, 11737–11744.
8. X. Han, Y. Ji and Y. Yang, *Advanced Functional Materials*, 2022, 32, 2109625.
9. J. K. Singh, S. K. Mandal and G. Banerjee, *Journal of Materials Research*, 2021, 36, 1773–1793.
10. D. Sando, C. Carrétéro, M. N. Grisolia, A. Barthélémy, V. Nagarajan and M. Bibes, *Advanced Optical Materials*, 2018, 6, 1700836.
11. A. K. Vishwakarma, P. Tripathi, A. Srivastava, A. S. K. Sinha and O. N. Srivastava, *International Journal of Hydrogen Energy*, 2017, 42, 22677–22686.
12. S. Yang, G. Ma, L. Xu, C. Deng and X. Wang, *RSC Advances*, 2019, 9, 29238–29245.
13. A. S. Priya, D. Geetha, J. M. Siqueiros and Ș. Țălu, *Molecules*, 2022, 27, 7565.

View Article Online
DOI: 10.1039/D6MA00329J

14. G. Kadim, R. Masrour and A. Jabar, *International Journal of Energy Research*, 2021, 45, 9961–9969.

15. Z. Arshad, S. Wageh, T. Maiyalagan, M. Ali, U. Arshad, M. B. Qadir, F. Mateen and A. G. Al-Sehemi, *Ceramics International*, 2022, 48, 24363–24371.

16. S. P. Madhusudanan, E. Balamoorthy, S. K. M, T. G. Manivasagam and S. K. Batabyal, *Journal of Solid State Electrochemistry*, 2022, 26, 2411–2421.

17. J. Kaur, O. Bethge, R. A. Wibowo, N. Bansal, M. Bauch, R. Hamid, E. Bertagnolli and T. Dimopoulos, *Solar Energy Materials and Solar Cells*, 2017, 161, 449–459.

18. R. Deepika and P. Meena, *Journal of Materials Science: Materials in Electronics*, 2023, 34, 16.

19. A. Raj, S. Sharma, D. V. Singh, A. Kumar, R. K. Chourasia, J. M. Siqueiros, O. R. Herrera, A. Anshul and M. Kumar, *Physica B: Condensed Matter*, 2024, 673, 415504.

20. S. Mazumder and K. Senthilkumar, *Solar Energy*, 2022, 237, 414–431.

21. S. Bhattarai, D. Borah, J. Rout, R. Pandey, J. Madan, I. Hossain, P. Handique, M. Z. Ansari, M. K. Hossain and M. F. Rahman, *RSC Advances*, 2023, 13, 34693–34702.

22. A. Kowsar, M. Shafayet-Ul-Islam, M. A. A. Shaikh, M. L. Palash, A. Kuddus, M. I. Uddin and S. F. U. Farhad, *Solar Energy*, 2023, 265, 112096.

23. P. Sriramalakshmi, *Results in Engineering*, 2025, 106180.

24. J. Madan, R. Pandey and R. Sharma, *Solar Energy*, 2020, 197, 212–221.

25. Z. Q. Wang, Z. H. Xiong, W. J. Hu, J. J. Jiang, Z. B. Cheng, Y. M. Xue, L. Peng and J. Lin, *Acta Physica Polonica A*, 2025, 147.

26. S. Abdelaziz, A. Zekry, A. Shaker and M. J. O. M. Abouelatta, *Optical Materials*, 2020, 101, 109738.

27. M. M. Mudassar, M. Arshad, M. U. Salman, M. Luqman, S. M. Ramay, M. Asim and S. Atiq, *Solar RRL*, 2026, 10, e202600009.

28. M. Sheikholeslami and Z. Khalili, *Sustainable Cities and Society*, 2024, 101, 105139.

29. J. Guerroum, M. Al-Hattab, Y. Chrafih, L. H. Moudou, K. Rahmani, Y. Lachtioui and O. Bajjou, *Solar Energy*, 2023, 266, 112194.

View Article Online
DOI: 10.1039/D6MA00329J

30. A. Owolabi, H. Ali, I. Musa, U. R. Ushiekpan, B. J. Akinade and M. L. Madugu, *Malaysian Journal of Applied Sciences*, 2021, 6, 69–84.
31. S. Yadav, P. Lohia and A. Sahu, *Journal of Optics*, 2024, 53, 3604–3616.
32. N. Rahman, M. D. Haque, M. F. Rahman, M. M. Islam, M. A. N. Juthi, A. R. Roy, M. A. Akter and M. F. Islam, *Discover Materials*, 2023, 3, 25.
33. M. Ameen, M. Bilal, M. U. Salman, M. Luqman, S. M. Ramay, W. Mahmood and S. Atiq, *RSC Advances*, 2025, 15, 25799–25810.
34. S. Sharma, R. Pandey, J. Madan and R. Sharma, *Optical Materials*, 2021, 111, 110644.
35. M. U. Salman, M. Bilal, Y. K. Karmani, U. Ali, S. M. Ramay, M. Younis and S. Atiq, *Journal of Materials Chemistry A*, 2025, 13, 15057–15066.
36. A. S. Abdullah, F. Ahmad, M. H. I. Ibrahim and M. H. Ibrahim, *Results in Optics*, 2024, 14, 100625.
37. J. P. A. Jebakumar, D. J. Moni, D. Gracia and M. D. Shallet, *Applied Nanoscience*, 2022, 12, 1507–1518.
38. U. C. Obi, D. M. Sanni and A. Bello, *Semiconductors*, 2021, 55, 922–927.
39. Y. Gan, D. Zhao, B. Qin, X. Bi, Y. Liu, W. Ning, R. Yang and Q. Jiang, *Energies*, 2022, 15, 7301.
40. E. Raza, J. Bhadra, M. Asif, F. Aziz, N. J. Al-Thani and Z. Ahmad, *Materials Today Communications*, 2023, 37, 107383.
41. M. K. Hossain, M. A. Islam, M. S. Uddin, P. Paramasivam, J. A. Hamid, R. A. Alshgari, V. K. Mishra and R. Haldhar, *Scientific Reports*, 2024, 14, 1–22.
42. R. Jeyakumar, A. Bag, R. Nekovei and R. Radhakrishnan, *Journal of Electronic Materials*, 2020, 49, 3533–3539.
43. Y. K. Karmani, M. Bilal, M. U. Salman, M. Ameen, M. Luqman, S. M. Ramay, M. Younis and S. Atiq, *Materials Science and Engineering B*, 2025, 321, 118484.
44. M. U. Salman, M. Mehak, U. Ali, G. M. U. Din, S. M. Ramay, M. Younis and S. Atiq, *RSC Advances*, 2025, 15, 15618–15629.
45. A. Amjad, S. Qamar, C. Zhao, K. Fatima, M. Sultan and Z. Akhter, *RSC Advances*, 2023, 13, 23211–23222.
46. M. Mottakin, D. K. Sarkar, V. Selvanathan, M. J. Rashid, K. Sobayel, A. M. Hasan, M. A. Islam, G. Muhammad, Shahiduzzaman and M. Akhtaruzzaman, *Optik*, 2023, 272, 170232.

View Article Online
DOI: 10.1039/D6MA00329J

47. D. Saikia, J. Bera, A. Betal and S. Sahu, *Optical Materials*, 2022, 123, 111839.
48. M. S. Reza, A. Ghosh, M. S. Reza, M. Aktarujjaman, M. J. Talukder, S. O. Aljazzar, J. Y. Al-Humaidi and Y. E. Mukhrish, *Langmuir*, 2025, 41, 6987–7007.
49. M. U. Salman and S. Atiq, *Materials Advances*, 2026, 7, 1604–1620.
50. G. Chen, J. Chen, W. Pei, Y. Lu, Q. Zhang, Q. Zhang and Y. He, *Materials Research Bulletin*, 2019, 110, 39–49.
51. D. Tiwari, D. J. Fermin, T. K. Chaudhuri and A. Ray, *The Journal of Physical Chemistry C*, 2015, 119, 5872–5877.
52. G. M. Mustafa, B. Younas, S. Saba, Z. M. Elqahtani, N. Alwadai and S. Aftab, *RSC Advances*, 2024, 14, 18957–18969.
53. W. A. Wani, H. Renuka, S. Kundu, S. Goel, H. Venkataraman and K. Ramaswamy, *Solar Energy*, 2022, 236, 822–831.
54. W. A. Wani, G. Gupta, S. Rath, H. Venkataraman and K. Ramaswamy, *Progress in Photovoltaics: Research and Applications*, 2024, 32, 556–568.
55. M. Arshad, M. M. Mudassar, M. U. Salman, I. Sagheer, S. M. Ramay, M. Asim and S. Atiq, *Journal of Power Sources*, 2026, 673, 239718.

View Article Online
DOI: 10.1039/D6MA00329J

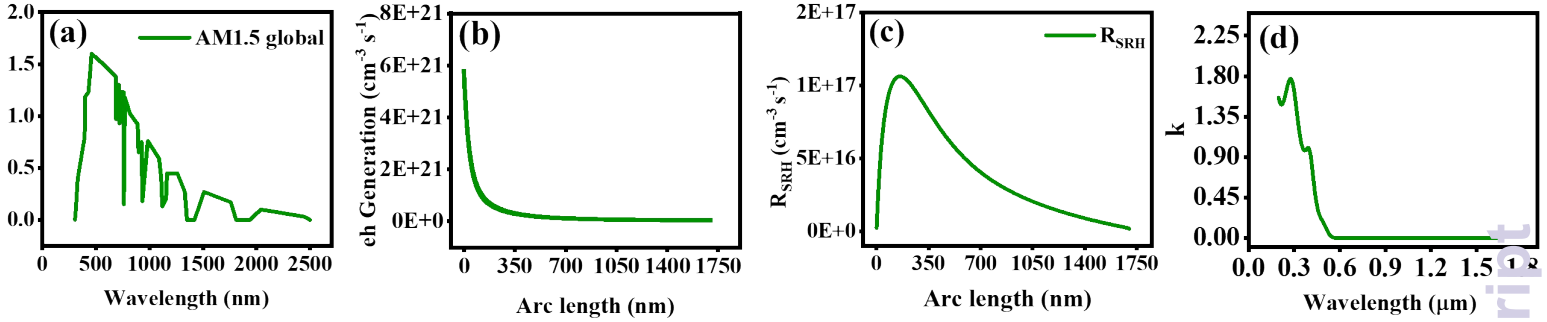

Figure 1(a) Solar irradiance spectrum (AirMass 1.5 Global) as a function of wavelength, **(b)** spatial distribution of electron-hole generation rate along the arc length, **(c)** Shockley-Read-Hall recombination rate (R_{SRH}) profile across the arc length, and **(d)** variation of extinction coefficient (k) with respect to wavelength.

View Article Online
DOI: 10.1039/D6MA00329J

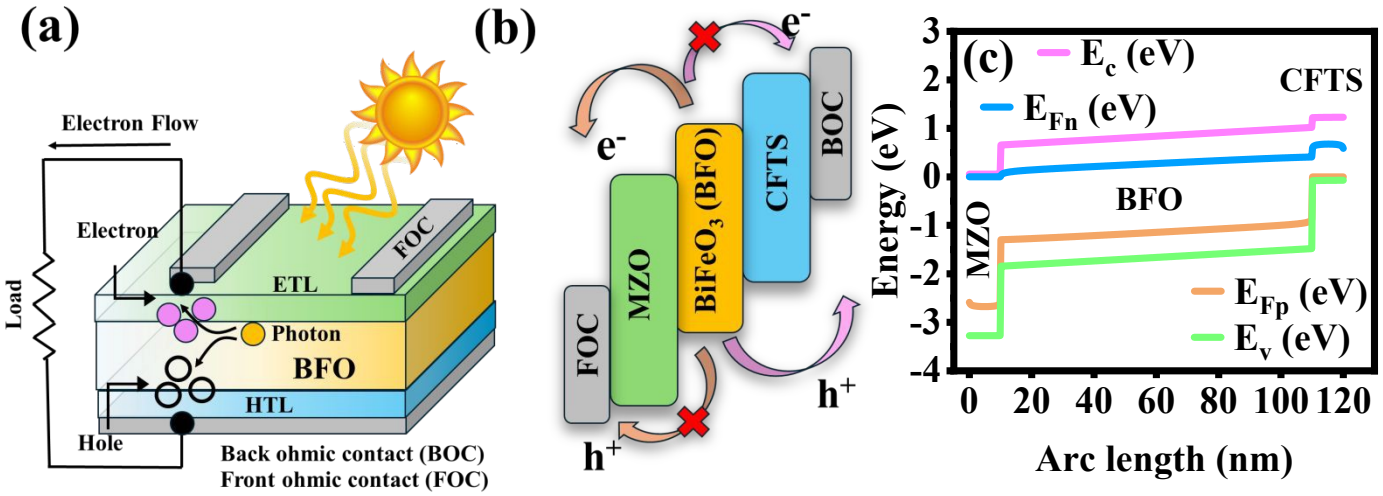

Figure 2(a) Schematic side view of the device architecture, illustrating the sequential stacking of individual layers of Mg-doped ZnO (ETL), BFO (absorbing layer), and CFTS (HTL), **(b)** top view of the solar cell layout, showing the flow of charge carriers across interfaces, and **(c)** energy band alignment of the device layers

View Article Online
DOI: 10.1039/D6MA00329J

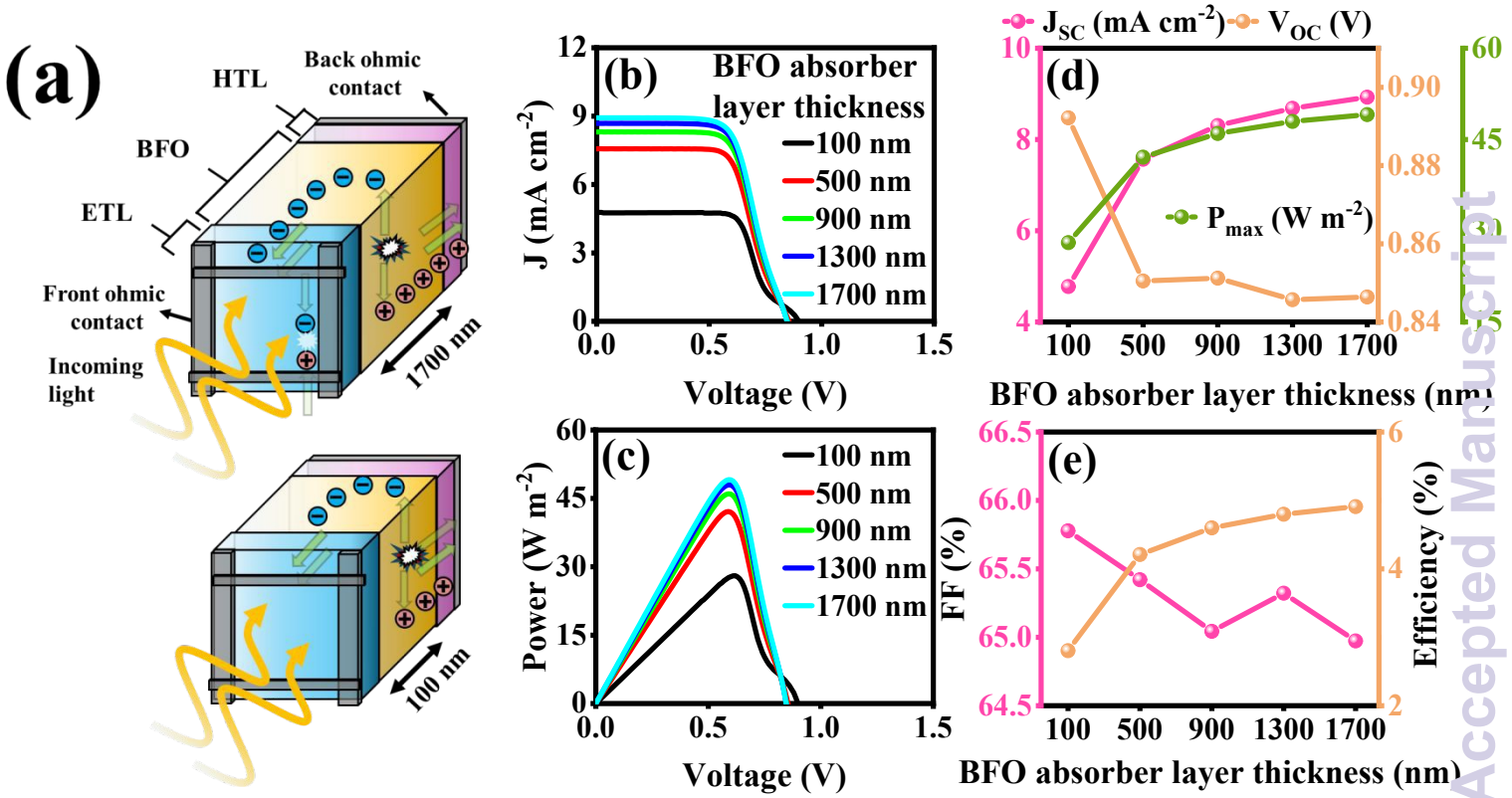

Figure 3 Effect of BFO absorber layer thickness on the photovoltaic performance of the Mg-ZnO/BFO/CFTS solar cell under standard illumination conditions, **(a)** schematic illustration of the variation in photogeneration rate with increasing BFO absorber layer thickness, showing enhanced carrier generation due to improved optical absorption in thicker layer and the effect of BFO absorber layer thickness on; **(b)** J-V characteristics, **(c)** P-V characteristics, **(d)** variation in J_{sc}, V_{oc}, and P_{max}, and **(e)** %FF and %efficiency.

View Article Online
DOI: 10.1039/D6MA00329J

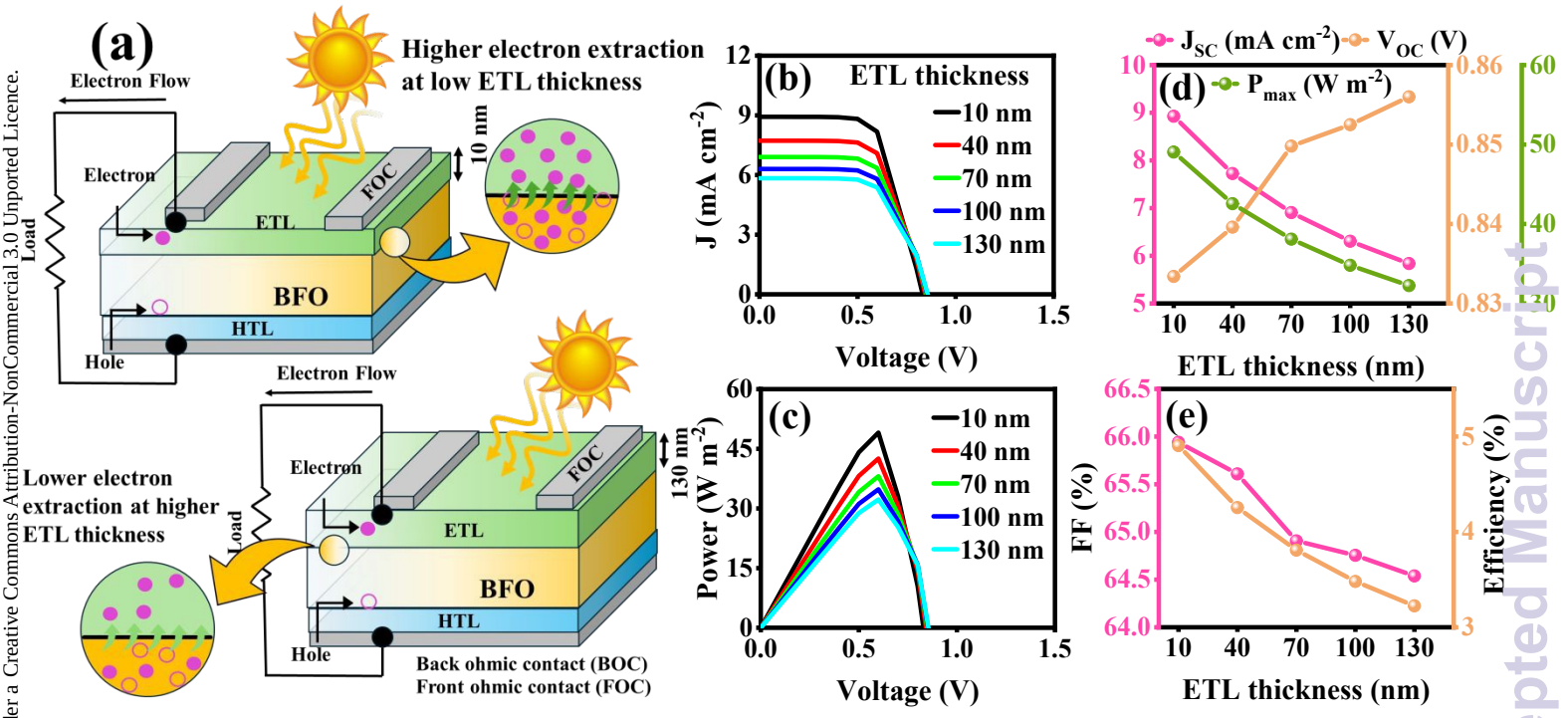

Figure 4 Effect of ETL thickness variation (10-130 nm) on the performance of the Mg-ZnO/BFO/CFTS solar cell under standard illumination conditions, **(a)** schematic representation of charge transport behavior showing improved electron extraction at lower ETL thickness due to reduced series resistance and enhanced carrier collection efficiency and the effect of ETL thickness on; **(b)** J-V curves, **(c)** P-V curves, **(d)** variation in J_{sc}, V_{oc}, P_{max}, and **(e)** %FF and %efficiency.

View Article Online
DOI: 10.1039/D6MA00329J

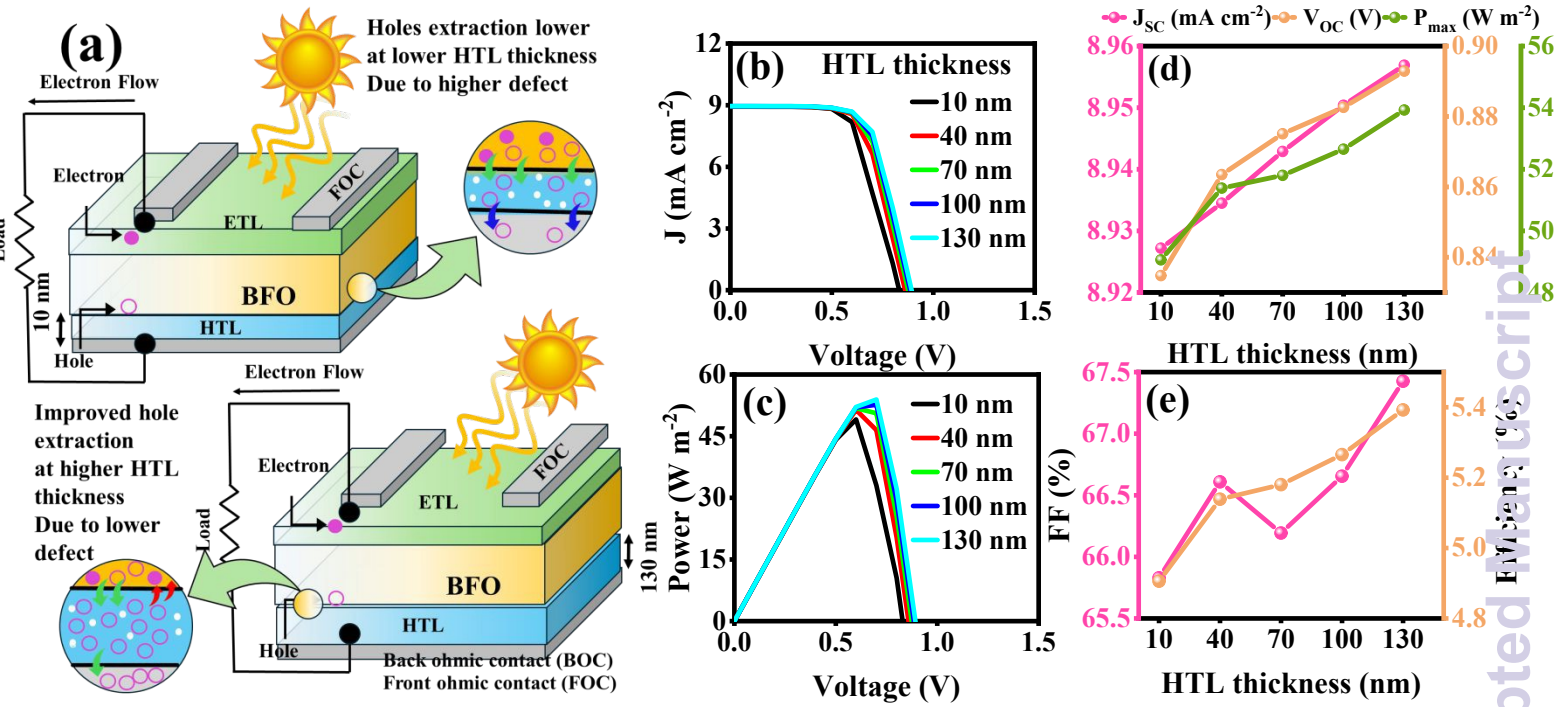

Figure 5 Effect of HTL thickness variation (10-130 nm) on the performance of the Mg-ZnO/BFO/CFTS solar cell under standard illumination conditions, **(a)** schematic illustration of hole transport behavior showing that reduced HTL thickness lower hole extraction due to higher defects, whereas excessive thickness improved hole extraction due to lower defects and the effect of HTL thickness on; **(b)** J-V curves, **(c)** P-V curves, **(d)** variation in J_{sc}, V_{oc}, P_{max}, and **(e)** %FF and %efficiency.

View Article Online
DOI: 10.1039/D6MA00329J

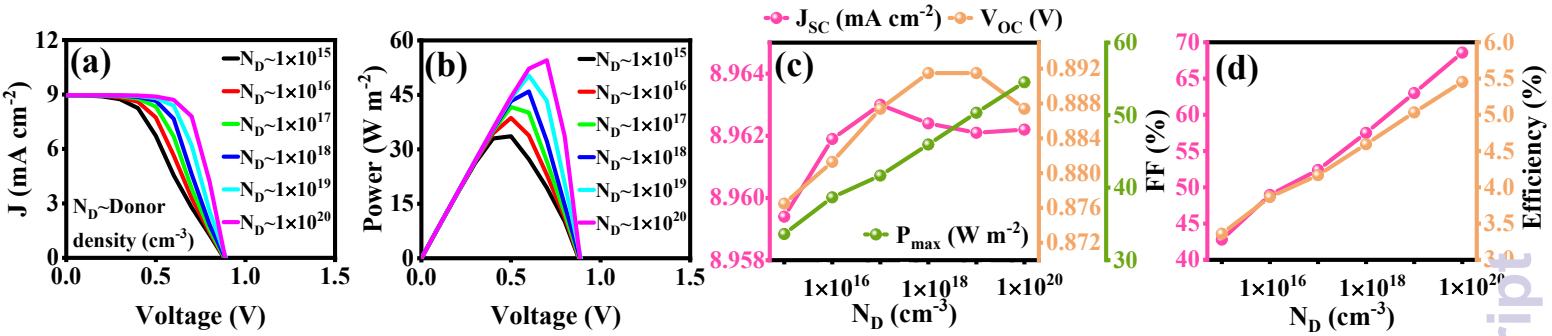

Figure 6 The effect of donor density (N_D) on; **(a)** J-V characteristics, showing improved output with increasing donor density, **(b)** P-V curves, illustrating enhancement in power extraction, **(d)** variation in J_{sc}, V_{oc}, P_{max}, and **(e)** trends in %FF and %efficiency

View Article Online
DOI: 10.1039/D6MA00329J

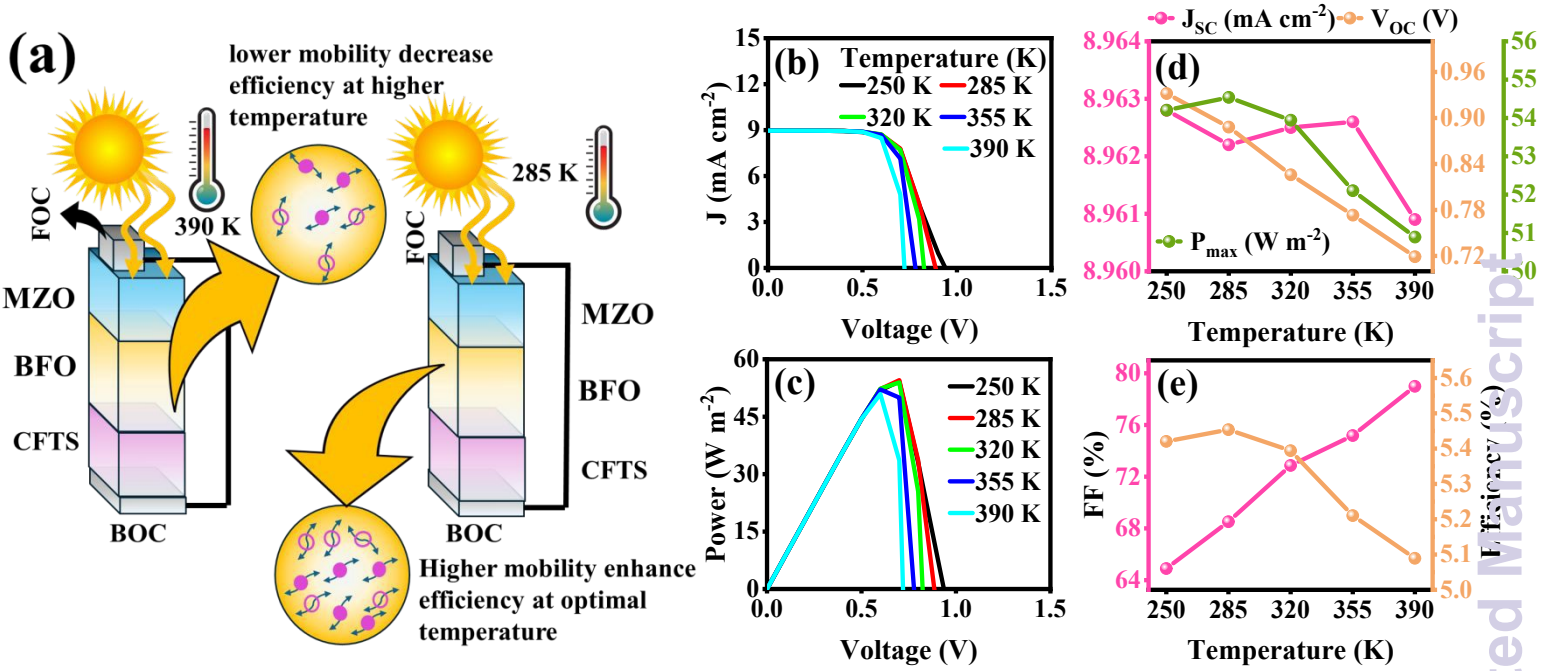

Figure 7 Effect of temperature variation on the photovoltaic performance of the Mg-ZnO/BFO/CFTS solar cell under standard illumination conditions, **(a)** schematic representation illustrating the temperature-dependent carrier transport behavior, where reduced lattice vibrations at lower temperature (285 K) enhance carrier mobility, while increased phonon scattering at higher temperature (350 K) leads to reduced mobility and degraded charge transport and the effect of temperature on; **(b)** J-V curves, **(c)** P-V curves, **(d)** variation in J_{sc}, V_{oc}, P_{max}, and **(e)** %FF and %efficiency.

View Article Online
DOI: 10.1039/D6MA00329J

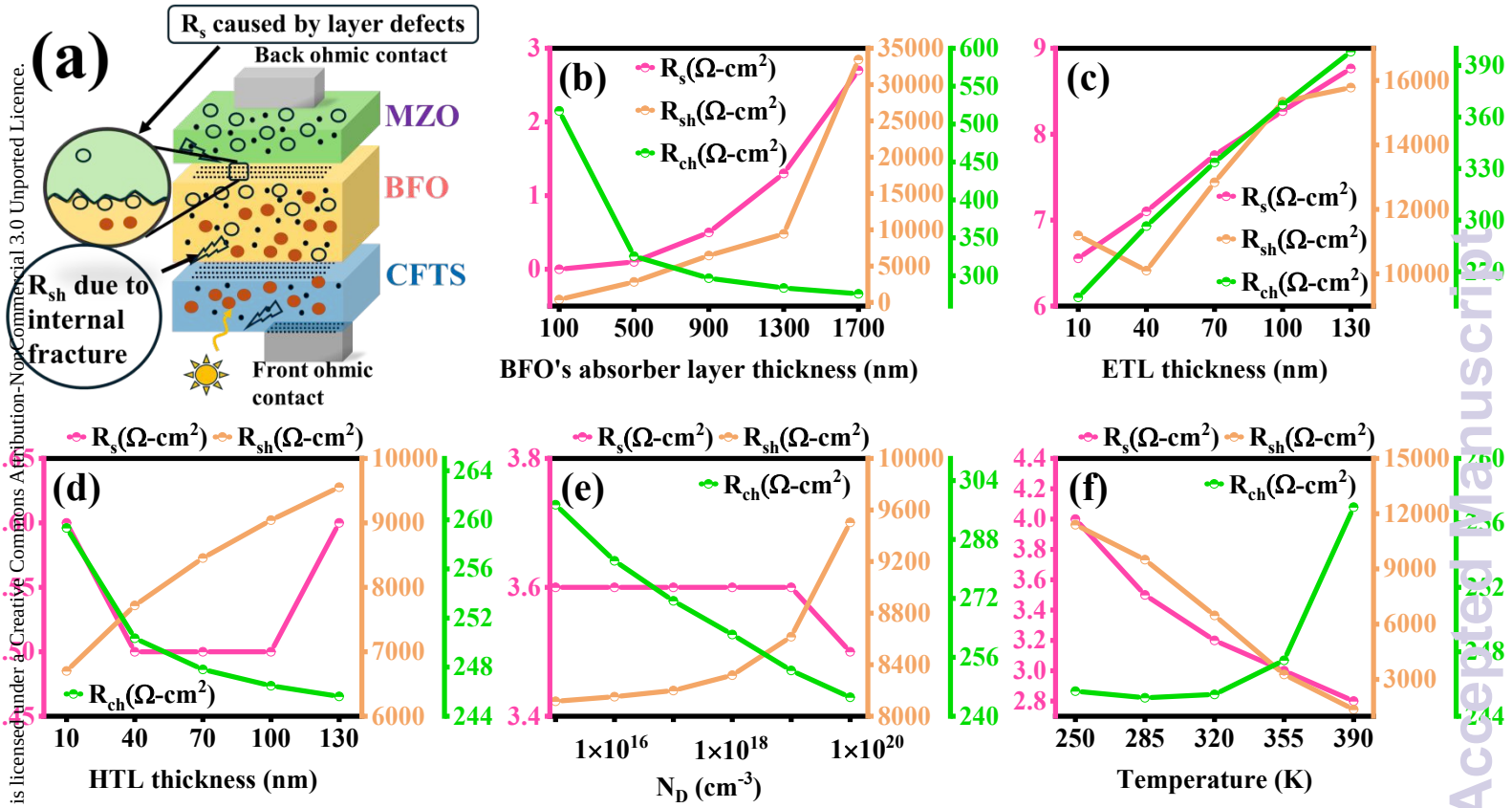

Figure 8(a) Schematic illustration of the origin of parasitic resistive components in the device, highlighting series resistance (R_s) arising from interfacial layer defects and shunt resistance (R_{sh}) originating from internal fractures and structural imperfections. The variation of R_s, R_{sh}, and characteristics resistance (R_{ch}) as a function of **(b)** BFO absorber layer thickness, **(c)** ETL thickness, **(d)** HTL thickness, **(e)** donor density (N_D), and **(f)** temperature.

View Article Online
DOI: 10.1039/D6MA00329J

Table 1 Initial optimized parameters used in COMSOL simulation for Mg-doped ZnO (MZO)/$BiFeO_3$ (BFO)/CFTS solar cell structure

Parameters	MZO (ETL)	$BiFeO_3$ (absorber layer)	CFTS (HTL)
Thickness (nm)	10	1700	10
Bandgap (eV)	3.33	2.5	1.3
Electron affinity (eV)	3.9	3.3	3.1
Dielectric constant	9	6	9
CB density of states (cm^{-3})	1×10^{21}	5.0×10^{19}	2.2×10^{18}
VB density of states (cm^{-3})	2×10^{20}	5.0×10^{19}	1.8×10^{19}
Mobility of e^- ($cm^2\ V^{-1}\ s^{-1}$)	20	80	21.98
Mobility of h^+ ($cm^2\ V^{-1}\ s^{-1}$)	10	25	21.98
Lifetime of e^- (ns)	1000	1000	1000
Lifetime of h^+ (ns)	1000	1000	1000
References	[34]	[35]	[36]

Table 2 Influence of BFO absorber layer thickness on the operational efficiency and output performance of MZO/$BiFeO_3$/CFTS solar cell under standard conditions

BFO absorber layer thickness (nm)	J_{sc} ($mA\ cm^{-2}$)	V_{oc} (V)	P_{max} ($W\ m^{-2}$)	FF %	Efficiency %
100	4.77	0.89	28.03	65.77	2.80
500	7.56	0.85	42.10	65.42	4.21
900	8.30	0.85	45.99	65.04	4.59
1300	8.68	0.84	47.97	65.32	4.79
1700	8.92	0.84	49.09	64.97	4.90

View Article Online
DOI: 10.1039/D6MA00329J

Table 3 Impact of ETL thickness variation on the photovoltaic performance parameters of $MZO/BiFeO_3/CFTS$ simulated solar cell

ETL thickness (nm)	J_{sc} (mA cm^{-2})	V_{oc} (V)	P_{max} (W m^{-2})	FF %	Efficiency %
10	8.92	0.83	49.05	65.94	4.90
40	7.72	0.83	42.55	65.60	4.25
70	6.90	0.84	38.09	64.90	3.80
100	6.30	0.85	34.80	64.75	3.48
130	5.83	0.85	32.24	64.53	3.22

Table 4 Influence of HTL thickness on the overall performance of $MZO/BiFeO_3/CFTS$ simulated solar cell

HTL thickness (nm)	J_{sc} (mA cm^{-2})	V_{oc} (V)	P_{max} (W m^{-2})	FF %	Efficiency %
10	8.92	0.83	49.05	65.82	4.90
40	8.93	0.86	51.38	66.60	5.13
70	8.94	0.87	51.80	66.19	5.18
100	8.95	0.88	52.65	66.65	5.26
130	8.95	0.89	53.92	67.42	5.39

Table 5 Variation in photovoltaic performance metrics of $MZO/BiFeO_3/CFTS$ solar cell with increasing donor density

Donor density (cm^{-3})	J_{sc} (mA cm^{-2})	V_{oc} (V)	P_{max} (W m^{-2})	FF %	Efficiency %
1×10^{15}	8.95	0.87	33.60	42.79	3.36
1×10^{16}	8.96	0.88	38.65	48.94	3.86
1×10^{17}	8.96	0.88	41.66	52.38	4.16
1×10^{18}	8.96	0.89	45.94	57.50	4.59
1×10^{19}	8.96	0.89	50.32	62.99	5.03
1×10^{20}	8.96	0.88	54.53	68.57	5.45

View Article Online
DOI: 10.1039/D6MA00329J

Table 6 Performance metrics tabulated as a function of temperature, highlighting the influence of thermal conditions on MZO/$BiFeO_3$/CFTS solar cell output

Temperature (K)	J_{sc} (mA cm^{-2})	V_{oc} (V)	P_{max} (W m^{-2})	FF %	Efficiency %
250	8.96	0.93	54.20	64.89	5.42
285	8.96	0.88	54.53	68.52	5.45
320	8.96	0.82	53.94	72.87	5.39
355	8.96	0.77	52.10	75.18	5.21
390	8.96	0.71	50.89	78.99	5.08

Table 7 Comparison of photovoltaic performance parameters for different BFO-based solar cell configurations with current work

Cell Structure	J_{sc} (mA cm^{-2})	V_{oc} (V)	FF %	Efficiency %
FTO/ZnO/BFO/spiro-OMeTAD/Au [19]	8.35	0.79	29.10	1.92
TiO_2/BFO/NiO [50]	0.51	0.67	55	0.19
Graphite/BFO/ZnO/ITO [51]	12.47	0.64	50.4	3.98
FTO/ BFO/GO (experimental) [52]	0.134	0.33	46.87	0.0207
AI/BFO/ITO (experimental) [53]	2.34	0.92	37	0.89
ITO/ZnO-uc/BFO/AI (experimental) [54]	4.7	0.89	53	2.21
MZO/BFO/CFTS [This work]	8.96	0.93	78.99	5.45

Table 8 Input and output optimized parameter values for this device

Optimized parameter	Optimized value	J_{sc} (mA cm^{-2})	V_{oc} (V)	P_{max} (W m^{-2})	FF %	Efficiency %
BFO absorber layer thickness	1700 nm	8.92	0.84	49.09	64.97	4.90
ETL thickness	10 nm	8.92	0.83	49.05	65.94	4.90
HTL thickness	130 nm	8.95	0.89	53.92	67.42	5.39
Donor density	1×10^{20} cm^{-3}	8.96	0.88	54.53	68.57	5.45
Temperature	285 K	8.96	0.88	54.53	68.52	5.45

View Article Online
DOI: 10.1039/D6MA00329J

Data Availability Statement

The data will be available on request.